GEOPHYSICS, VOL. 83, NO. 4 (JULY-AUGUST 2018); P. IM29–IM40, 12 FIGS.
10.1190/GEO2017-0830.1

Least-squares horizons with local slopes and multigrid correlations

Xinming Wu[1] and Sergey Fomel[1]

ABSTRACT

Most seismic horizon extraction methods are based on seismic local reflection slopes that locally follow seismic structural features. However, these methods often fail to correctly track horizons across discontinuities such as faults and noise because the local slopes can only correctly follow laterally continuous reflections. In addition, seismic amplitude or phase information is not used in these methods to compute horizons that follow a consistent phase (e.g., peaks or troughs). To solve these problems, we have developed a novel method to compute horizons that globally fit the local slopes and multigrid correlations of seismic traces. In this method, we first estimate local reflection slopes by using structure tensors and compute laterally multigrid slopes by using dynamic time warping (DTW) to correlate seismic traces within multiple laterally coarse grids. These coarse-grid slopes can correctly correlate reflections that may be significantly dislocated by faults or other discontinuous structures. Then, we compute a horizon by fitting, in the least-squares sense, the slopes of the horizon with the local reflection slopes and multigrid slopes or correlations computed by DTW. In this least-squares system, the local slopes on the fine grid and the multiple coarse-grid slopes will fit a consistent horizon in areas without lateral discontinuities. Across laterally discontinuous areas where the local slopes fail to correctly correlate reflections and mislead the horizon extraction, the coarse-grid slopes will help to find the corresponding reflections and correct the horizon extraction. In addition, the multigrid correlations or slopes computed by dynamic warping can also assist in computing phase-consistent horizons. We apply the proposed horizon extraction method to multiple 2D and 3D examples and obtain accurate horizons that follow consistent phases and correctly track reflections across faults.

INTRODUCTION

By laterally tracking consistent seismic reflections, we are able to identify horizons from seismic images. Seismic horizons are often considered as geologically synchronous surfaces (Vail et al., 1977), which are important for building subsurface structural and stratigraphic models. Seismic attribute features computed on a horizon surface are also helpful for seismic geomorphology analysis (Posamentier et al., 2007). Therefore, seismic horizon interpretation has been a common and key step for seismic interpretation.

Numerous methods have been proposed to automatically or semiautomatically extract horizons from seismic images. Some methods are based on seismic instantaneous phase by assuming a horizon is a curve (two dimensions) or surface (three dimensions) that follows relatively constant phase through the whole seismic image. In these phase-based methods, the instantaneous phases are first unwrapped to obtain a relative geologic time (RGT) volume and the horizons are then extracted as contours of the RGT values (Stark, 2003, 2004, 2005; Wu and Zhong, 2012). Some other methods are based on seismic waveform classifications. In these methods, a horizon is gradually grown from a seed point by recursively following waveforms with the most similarities (Figueiredo et al., 2007, 2014, 2015).

Most horizon extraction methods are based on seismic local reflection slopes that estimate the geometric orientations of reflections. The local reflection slopes can be estimated by using structure tensors (Bakker et al., 1999; Bakker, 2002; Hale, 2009b; Wu and Janson, 2017), plane-wave destruction filters (Fomel, 2002), semblance scanning (Marfurt, 2006), 2D log-Gabor filtering (Yu et al., 2013), and smooth dynamic image warping (Arias, 2016). The local slopes can correctly follow laterally continuous reflections, but they often fail to correlate significantly displaced reflections across faults. A straightforward slope-based horizon extraction method is to pick horizons by starting from seed points and then recursively following the local slopes (Fomel, 2010). Most slope-based methods (e.g., Lomask et al., 2006; Parks, 2010; Wu and Hale, 2013,

Manuscript received by the Editor 20 December 2017; revised manuscript received 24 February 2018; published ahead of production 27 April 2018; published online 25 June 2018.
[1]The University of Texas at Austin, Bureau of Economic Geology, Austin, Texas, USA. E-mail: xinming.wu@beg.utexas.edu; sergey.fomel@beg.utexas.edu.

2015; Zinck et al., 2013; Monniron et al., 2016) compute horizons by fitting the slopes of horizons with the local reflection slopes in the least-squares sense. By recursively following local slopes or fitting local slopes in the least-squares sense, the computed horizons can correctly follow laterally continuous reflections but they often fail to track corresponding reflections across faults because the local slopes cannot correctly correlate reflections across faults. To solve this problem, methods are proposed to remove the faulting (Luo and Hale, 2013; Wu and Hale, 2016; Wu et al., 2016) in the seismic images before computing horizons or to incorporate manual control points (Wu and Hale, 2015) (on the opposite sides of faults) as constraints during the horizon computation.

We propose a new method to accurately extract horizons across faults without the need of removing faulting or manually picking control points across faults. In our method, we first use structure tensors to estimate the linearity (two dimensions) or planarity (three dimensions) and local slopes of seismic reflections. The linearity or planarity highlights reflection discontinuities with relatively low values. We also compute laterally multigrid slopes by directly correlating seismic traces within multiple laterally coarse grids. These multigrid slopes can help to correlate reflections across faults and find consistent phase correlations of the seismic traces. Then, we compute horizons by fitting, in the least-squares sense, the slopes of horizons with the local reflection slopes and multigrid slopes. In areas without faults, the local slopes and coarse-grid slopes will be consistent to fit a horizon. Near faults where the local slopes fail to correctly correlate reflections, the local slopes are weighted by low linearity or planarity values in the least-squares system. By doing this, we are able to reduce their relative influence in the least-squares system and allow the coarse-grid slopes, that correctly correlate reflection slopes across faults, to contribute more to fit a correct horizon across faults. In addition, the multigrid slopes or correlations can be helpful to constrain the horizon extraction to follow consistent phases. We show multiple 2D and 3D examples with faults to demonstrate the proposed method with the local slopes and multigrid correlations, which yields much more accurate horizons than the conventional methods that use only local slopes.

SLOPES AND CORRELATIONS

Seismic reflection slopes are important for most automatic methods to extract horizons following seismic reflections. The slopes can be estimated by numerous methods including structure tensors (Bakker et al., 1999; Bakker, 2002; Hale, 2009b), plane-wave destruction (Fomel, 2002), semblance scanning (Marfurt, 2006), 2D log-Gabor filtering (Yu et al., 2013), and smooth dynamic image warping (Arias, 2016). In this paper, we use structure tensors to estimate local reflection slopes for seismic horizon extraction.

Structure tensors

Structure tensors, first proposed for common digital image processing (e.g., Van Vliet and Verbeek, 1995; Weickert, 1997), have been widely used in estimating seismic structural (Bakker, 2002; Fehmers and Höcker, 2003; Hale, 2009b) and stratigraphic (Wu, 2017; Wu and Janson, 2017) orientations.

Structure tensors are generally constructed as smoothed outer products of gradients $\mathbf{g}(\mathbf{x})$ of an image such as the one shown in Figure 1a. In 2D cases, a structure tensor $\mathbf{T}(\mathbf{x})$ field at all image samples $\mathbf{x}$ can be computed as

$$\mathbf{T}(\mathbf{x}) = \begin{bmatrix} \langle g_1(\mathbf{x})g_1(\mathbf{x})\rangle & \langle g_1(\mathbf{x})g_2(\mathbf{x})\rangle \\ \langle g_1(\mathbf{x})g_2(\mathbf{x})\rangle & \langle g_2(\mathbf{x})g_2(\mathbf{x})\rangle \end{bmatrix}, \tag{1}$$

where $g_1(\mathbf{x})$ and $g_2(\mathbf{x})$, respectively, represent the vertical and horizontal components of the image gradients $\mathbf{g}(\mathbf{x})$. The structure tensor field contains three independent components $g_1^2(\mathbf{x})$, $g_1(\mathbf{x})g_2(\mathbf{x})$, and $g_2^2(\mathbf{x})$, each of which can be considered as a 2D image with the same dimensions as the input image. $\langle\cdot\rangle$ represents 2D smoothing of each component of the structure tensor field. This smoothing $\langle\cdot\rangle$ is often implemented as a Gaussian filter. In all 2D examples in this paper, we implement the smoothing $\langle\cdot\rangle$ by using 2D recursive Gaussian smoothing filters (Hale, 2006) with half-widths $\sigma_1 = 8$ (samples) and $\sigma_2 = 2$ (samples) in the vertical and inline directions, respectively. We use a larger vertical smoothing window because the vertical sampling is often finer than the horizontal sampling in a seismic image.

The structure tensors constructed in this way (equation 3) are 2×2 symmetric positive-semidefinite matrices with the following eigendecompositions:

$$\mathbf{T} = \lambda_u \mathbf{u}\mathbf{u}^\top + \lambda_v \mathbf{v}\mathbf{v}^\top, \tag{2}$$

where $\mathbf{u}$ and $\mathbf{v}$ are the normalized eigenvectors corresponding the eigenvalues λ_u and λ_v, respectively. By assuming $\lambda_u \geq \lambda_v$, the corresponding eigenvectors $\mathbf{u}(\mathbf{x})$ will be perpendicular to seismic reflections whereas the eigenvectors $\mathbf{v}(\mathbf{x})$ will be parallel to the reflections.

In 3D cases, a structure tensor $\mathbf{T}(\mathbf{x})$ field at all image samples $\mathbf{x}$ can be constructed as

$$\mathbf{T}(\mathbf{x}) = \begin{bmatrix} \langle g_1(\mathbf{x})g_1(\mathbf{x})\rangle & \langle g_1(\mathbf{x})g_2(\mathbf{x})\rangle & \langle g_1(\mathbf{x})g_3(\mathbf{x})\rangle \\ \langle g_1(\mathbf{x})g_2(\mathbf{x})\rangle & \langle g_2(\mathbf{x})g_2(\mathbf{x})\rangle & \langle g_2(\mathbf{x})g_3(\mathbf{x})\rangle \\ \langle g_1(\mathbf{x})g_3(\mathbf{x})\rangle & \langle g_2(\mathbf{x})g_3(\mathbf{x})\rangle & \langle g_3(\mathbf{x})g_3(\mathbf{x})\rangle \end{bmatrix}, \tag{3}$$

where we implement the smoothing $\langle\cdot\rangle$ by using 3D recursive Gaussian filters with half-widths $\sigma_1 = 8$ (samples), $\sigma_2 = 2$ (samples), and $\sigma_3 = 2$ (samples) in the vertical, inline, and crossline directions, respectively. Similarly, the eigendecompositions of 3D structure tensors can provide the orientation estimation of seismic reflections:

$$\mathbf{T} = \lambda_u \mathbf{u}\mathbf{u}^\top + \lambda_v \mathbf{v}\mathbf{v}^\top + \lambda_w \mathbf{w}\mathbf{w}^\top, \tag{4}$$

where the normalized eigenvectors $\mathbf{u}$ are perpendicular to seismic reflections, whereas the eigenvectors $\mathbf{v}$ and $\mathbf{w}$ are aligned within planes that are locally parallel to the reflections.

The eigenvalues $\lambda_u(\mathbf{x})$, $\lambda_v(\mathbf{x})$, and $\lambda_w(\mathbf{x})$ are also useful to measure the anisotropy of seismic reflections such as the linearity (two dimensions) or planarity (three dimensions) as follows (Hale, 2009b; Wu, 2017):

$$c(\mathbf{x}) = \frac{\lambda_u(\mathbf{x}) - \lambda_v(\mathbf{x})}{\lambda_u(\mathbf{x})}. \tag{5}$$

As shown in Figure 1b, the linearity map $c(\mathbf{x})$ ($0 \leq c(\mathbf{x}) \leq 1$) can be used to highlight reflection discontinuities at faults where the linearity will be lower.

Reflection slopes

Assuming that the reflection normal vectors $\mathbf{u}(\mathbf{x})$ are always pointing downward, we can compute inline and crossline reflection slopes from the normal vectors as follows:

$$p(\mathbf{x}) = -\frac{u_2(x)}{u_1(\mathbf{x})} \quad \text{and} \quad q(\mathbf{x}) = -\frac{u_3(x)}{u_1(\mathbf{x})}, \tag{6}$$

where $u_1(\mathbf{x})$, $u_2(\mathbf{x})$, and $u_3(\mathbf{x})$, respectively, are the vertical, inline, and crossline components of the vectors $\mathbf{u}(\mathbf{x})$. Accordingly, $p(\mathbf{x})$ and $q(\mathbf{x})$ represent the inline and crossline reflection slopes, respectively.

The cyan segments in Figure 1c represent a subset of the slope vectors $[p(\mathbf{x}), 1]$, which correctly follow locally continuous reflections. The slopes $p(\mathbf{x})$, estimated from structure tensors, can be actually considered as relatively vertical shifts that correlate nearby seismic traces. These estimated slopes can correctly correlate laterally continuous reflections of nearby traces, but often fail to correlate laterally discontinuous reflections that may be significantly dislocated by faults or noise.

To estimate large relative shifts of reflections across faults, we can directly correlate the seismic traces on the opposite sides of faults by using the methods of crosscorrelation (Hale, 2009a), local similarity (Fomel and Jin, 2009), or dynamic time warping) (Hale, 2013). The two vertical yellow lines in Figure 1d represent two seismic traces $\mathbf{f}$ and $\mathbf{g}$ that are on opposite sides of the large-displacement fault highlighted by the yellow line in Figure 1a. By locally following the local slope vectors shown in Figure 1c, we will not be able to find the correct correlations of these two traces. However, we can use the DTW method to directly compute accurate correlations of the two traces as denoted by the red lines in Figure 1d.

Dynamic time warping

The DTW method is first proposed by Sakoe and Chiba (1978) in speech recognition, and then it is widely used in geophysics to correlate well logs (e.g., Smith and Waterman, 1980; Wu and Nyland, 1987; Julio et al., 2012; Wheeler and Hale, 2014; Wu et al., 2017) and seismic traces or images (e.g., Hale, 2013; Herrera and van der Baan, 2014; Wu and Caumon, 2017). DTW is robust to estimate correlation shifts in the presence of noise, and it is often more accurate than windowed crosscorrelation methods, especially in estimating rapidly varying shifts (Hale, 2013).

To compute the correlation shifts $\mathbf{s} = (s_1, s_2, \ldots, s_n)$ of two sequences, such as the two seismic traces $\mathbf{f} = (f_1, f_2, \ldots, f_n)$ and $\mathbf{g} = (g_1, g_2, \ldots, g_n)$ extracted from the 2D seismic section (Figure 1d), DTW solves the following constrained minimization problem:

$$\arg\min_{\mathbf{s}} \sum_{i=1}^{n} (f_i - g_{i+s_i})^2 \quad \text{subject to } |s_i - s_{i-1}| \le \varepsilon, \tag{7}$$

where the shift strain $0 < \varepsilon \le 1$ defines squeezing ($s_i - s_{i-1} < 0$) or stretching ($s_i - s_{i-1} > 0$) (Hale, 2013) in shifting one sequence to the other.

With the shifts $\mathbf{s} = (s_1, s_2, \ldots, s_n)$ computed from the DTW method, we are able to build pair-wise correlations between all the samples in the seismic traces $\mathbf{f}$ and $\mathbf{g}$. The red lines in Figures 1d and 2 denote a subset of such pair-wise correlations, which correctly link geologically corresponding reflections as shown in Figure 1d.

In the following sections, we will use structure tensors to estimate local slopes of reflections and use DTW to estimate laterally more global correlations of reflections on coarse grids. We further formulate a weighted least-squares system to compute a horizon that is consistent with local and global correlations.

HORIZONS WITH LOCAL SLOPES

With the estimated local reflection slopes, a straightforward way of picking horizons is to start with seed points and then predictively follow the local slopes (Fomel, 2010). Another commonly used way of slope-based horizon picking is to globally fit horizon slopes with the preestimated local reflection slopes in the least-squares sense (e.g., Lomask et al., 2006; Parks, 2010; Wu and Hale, 2013, 2015).

Predictive horizons with local slopes

To extract a 2D horizon curve $z(x)$ following reflection slopes, we expect the slopes of the horizon to be equal to the reflection slopes:

$$\frac{\partial z(x)}{\partial x} = p(x, z(x)), \quad \text{subject to } z(x_0) = z_0, \tag{8}$$

where the slopes of the horizon $z(x)$ are computed as the first derivatives on the left side. The reflection slopes p on the right side are precomputed from the seismic image using structure tensors. The seed point (x_0, z_0) defines a position at which the horizon must pass through.

A direct way to solve the above equation 8 is to start with the seed point (x_0, z_0) and recursively accumulate the local reflection slopes:

$$z(x_{i+1}) = z(x_i) + p(x_i, z(x_i)), \quad i \in \{0, 1, 2, \ldots, m-1\}, \tag{9}$$

where x_m defines a bound where the horizon will end. Such a direct way of slope-based horizon picking is highly efficient to pick the horizons (yellow curves) shown in Figure 3a, where the red circles denote the seed points for the horizons.

However, this recursive accumulation method is path-dependent in picking a 3D horizon surface. The picked horizon can significantly vary with different accumulation paths, and errors will propagate with the path to yield a highly unstable horizon, if the estimated slopes contain noise. Because of the error propagations, all the horizons except the top one in Figure 3a keep going further away from the correct positions when growing the horizons away from the seed points. Another disadvantage of this method is that it is inconvenient to incorporate multiple seed points into this method to generate a single horizon conforming to all of the points.

Least-squares horizons with local slopes

A more stable way of slope-based horizon picking is to compute a weighted least-squares fit of the horizon slopes with the preesti-

mated reflection slopes (Lomask et al., 2006; Wu and Hale, 2013, 2015; Zinck et al., 2013). In cases in which the estimated reflection slopes are highly noisy, we can further impose smooth regularizations on the horizon and build the following equations for the 2D slope-based horizon extraction:

$$\begin{bmatrix} w(x,z(x))\frac{\partial z(x)}{\partial x} \\ \mu\frac{\partial^2 z(x)}{\partial x^2} \end{bmatrix} \approx \begin{bmatrix} w(x,z(x))p(x,z(x)) \\ 0 \end{bmatrix}, \qquad (10)$$

where the weighting map $0 \le w(x,z) \le 1$ represents some kind of quality measurement of the estimated reflection slopes. We define such a quality map with the reflection linearity image shown in Figure 1b. In the linearity image, the relatively low values are mostly apparent in areas with noise or discontinuous reflections, where

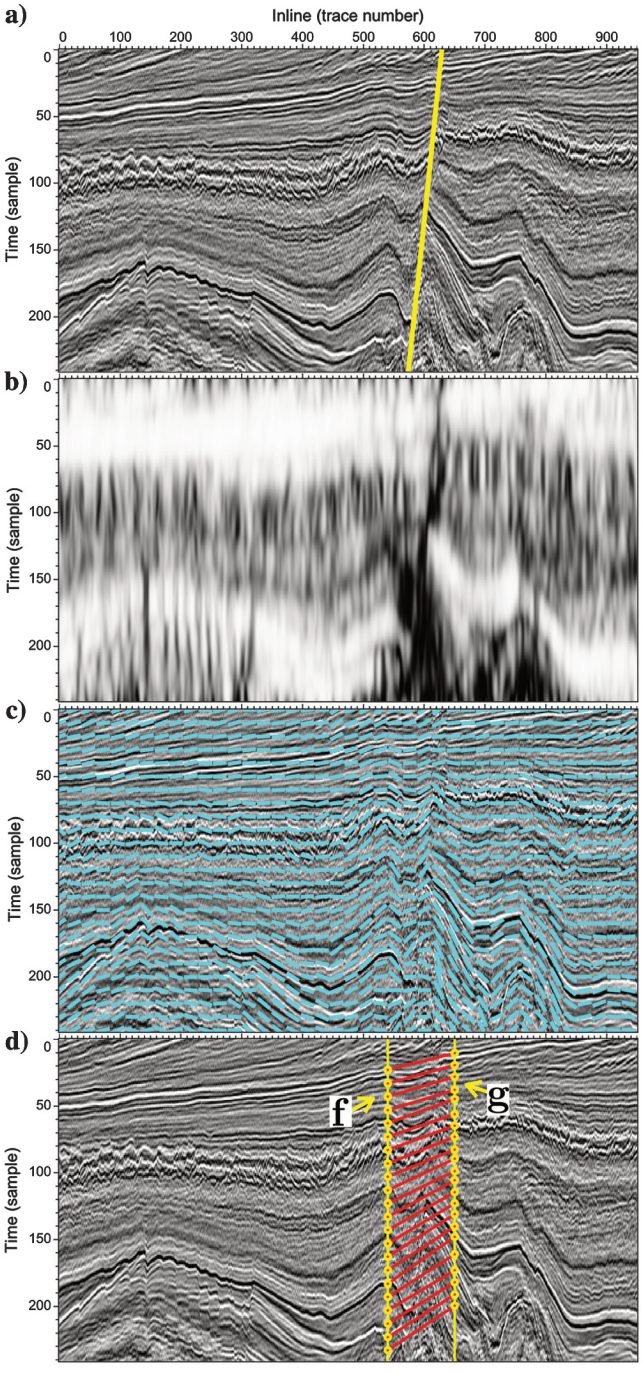

Figure 1. (a) From a 2D seismic image, we use structure tensors to simultaneously estimate (b) linearity and (c) slopes of seismic reflections. The linearity highlights reflection discontinuities with relatively low values. (d) The slopes locally follow laterally continuous reflections, but they fail to correlate reflections across faults, where we can use DTW to directly correlate seismic traces on the opposite sides of the faults.

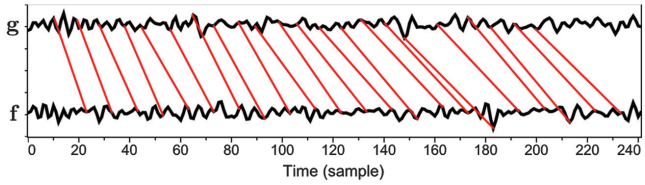

Figure 2. Two seismic traces are correlated by DTW.

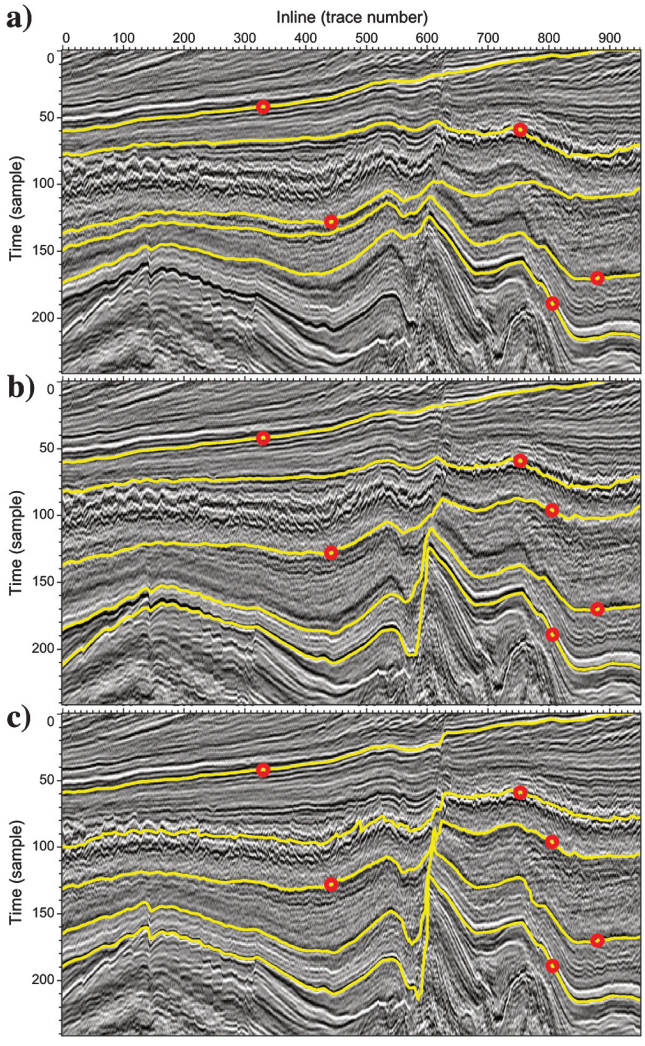

Figure 3. (a) A 2D seismic image is displayed with five horizons that are extracted by predictively following local slopes, (b) least-squares fitting of only local slopes, and (c) least-squares fitting of local slopes and multigrid correlations, respectively.

reflection slopes are often poorly estimated. The second equation is a regularization term to impose smoothness on the horizon to be computed, and μ is a small constant ($\mu = 0.001$), which gives a trade-off between smoothness and honoring local slopes.

Note that the weight $w(x, z(x))$ and slope $p(x, z(x))$ on the right side are dependent on the unknown horizon $z(x)$, which means that equation 10 is nonlinear. As we initially do not know the correct position of the horizon, we must start with some user-defined initial guess of the horizon $z_0(x)$ and then iteratively update the horizon as follows:

$$\begin{bmatrix} w(x, z_i)\frac{\partial z_{i+1}}{\partial x} \\ \mu\frac{\partial^2 z_{i+1}}{\partial x^2} \end{bmatrix} \approx \begin{bmatrix} w(x, z_i)p(x, z_i) \\ 0 \end{bmatrix}. \quad (11)$$

In this iterative scheme of computing the horizon $z_{i+1} = z_{i+1}(x)$ at the ith iteration, we use the weights $w(x, z_i(x))$ and reflection slope $p(x, z_i(x))$ on the previously updated horizon $z_i = z_i(x)$ to define equation 11. We can rewrite it in the matrix-vector form as follows:

$$\begin{bmatrix} \mathbf{W}_i\mathbf{D}_x\mathbf{z}_{i+1} \\ \mu\mathbf{D}_{xx}\mathbf{z}_{i+1} \end{bmatrix} = \begin{bmatrix} \mathbf{W}_i\mathbf{p}_i \\ \mathbf{0} \end{bmatrix}, \quad (12)$$

where the diagonal matrix $\mathbf{W}_i$ contains the weights, vector $\mathbf{p}_i$ contains the reflection slopes, and matrices $\mathbf{D}_x$ and $\mathbf{D}_{xx}$ represent finite-difference approximations of the first and second derivatives, respectively. To update horizon $\mathbf{z}_{i+1}$ at the ith iteration, we compute the least-squares solution to the above equation by solving the corresponding normal equation as follows:

$$(\mathbf{D}_x^\top\mathbf{W}_i^2\mathbf{D}_x + \mu^2\mathbf{D}_{xx}^\top\mathbf{D}_{xx})\mathbf{z}_{i+1} = \mathbf{D}_x^\top\mathbf{W}_i^2\mathbf{p}_i. \quad (13)$$

In this iterative scheme of computing a horizon, we begin with an initial horizon and solve a sequence of such a least-squares equation 13 to iteratively update the horizon until the average updating is smaller than some small threshold $(1/N)\sum_{j=0}^{N}|z_{i+1}(x_j) - z_i(x_j)| \le \varepsilon$. As discussed by Wu and Hale (2015), multiple control points can be conveniently incorporated as hard constraints into this method by solving the following constrained equation at each iteration:

$$(\mathbf{D}_x^\top\mathbf{W}_i^2\mathbf{D}_x + \mu^2\mathbf{D}_{xx}^\top\mathbf{D}_{xx})\mathbf{z}_{i+1} = \mathbf{D}_x^\top\mathbf{W}_i^2\mathbf{p}_i,$$
$$\text{subject to } \mathbf{z}_{i+1}[k_c] = z_c, c = \{1, 2, \ldots, K\}, \quad (14)$$

where k_c represent the indexes corresponding to the lateral positions of the control points and z_c are the known depth positions of the control points. As discussed by Wu and Hale (2015), such a constrained least-squares problem can be efficiently solved by using a conjugate gradient solver with a constraint preconditioner and starting with an initial horizon passing through the control points.

The iterative scheme of 2D horizon picking (equation 11) can be easily extended for iteratively computing a 3D horizon surface $z_{i+1}(x, y)$:

$$\begin{bmatrix} w(x, y, z_i)\frac{\partial z_{i+1}}{\partial x} \\ w(x, y, z_i)\frac{\partial z_{i+1}}{\partial y} \\ \mu\left(\frac{\partial^2 z_{i+1}}{\partial x^2} + \frac{\partial^2 z_{i+1}}{\partial y^2}\right) \end{bmatrix} \approx \begin{bmatrix} w(x, y, z_i)p(x, y, z_i) \\ w(x, y, z_i)q(x, y, z_i) \\ 0 \end{bmatrix}, \quad (15)$$

where $p(x, y, z_i(x, y))$ and $q(x, y, z_i(x, y))$, respectively, represent the precomputed inline and crossline reflection slopes that are extracted on the positions of the previously updated horizon surface $z_i(x, y)$. Similar to what we do for 2D horizon picking, we compute the least-squares solution of this equation 15 and incorporate control points by solving the following constrained equation:

$$(\mathbf{G}^\top\mathbf{W}_i^2\mathbf{G} + \mu^2\mathbf{L}^\top\mathbf{L})\mathbf{z}_{i+1} = \mathbf{G}^\top\mathbf{W}_i^2\mathbf{p}_i,$$
$$\text{subject to } \mathbf{z}_{i+1}[k_c] = z_c, c = \{1, 2, \ldots, K\}, \quad (16)$$

where $\mathbf{G}$ and $\mathbf{L}$ are matrices representing the finite-difference approximations of 2D gradient and Laplace operators, respectively.

By using the 2D iterative scheme of least-squares fitting of slopes (equation 14), we compute the five horizons (yellow curves) with one or two control points (red cycles) as shown in Figure 3b. In computing a horizon with only one control point, we start with an initial horizon that is a horizontal line passing through the control point. In computing a horizon with two or more control points, we start with an initial horizon that is a curve interpolated from the control points. All these horizons converge to the final positions (shown in Figure 3b) after five iterations. We observe that these horizons are still not accurately extracted because the estimated slopes cannot correctly correlate reflections across faults. However, these horizons are closer to the correct positions than those computed in Figure 3a.

Figure 4a shows another 2D example, which is also complicated by many faults. The cyan segments in Figure 4b represent the estimated slope vectors, which, again, locally follow the continuous reflections, but they fail to correlate the reflections across faults. Figure 4c shows the iterative horizon extraction, where we begin with an initially horizontal line (blue line) passing through the control point (the yellow circle) and then gradually update the horizon by fitting the horizon slopes with the reflection slopes in the least-squares sense at each iteration. The horizons updated at the third (the orange curve), fourth (the magenta curve), and fifth (the red curve) iterations are overlaid with each other, which means that the horizon already converges at the fourth iteration. However, this finally updated horizon does not converge to the correct position because of slope errors near the faults. In the next section, we will discuss how to further improve the iterative horizon extraction (Figures 3c and 4d) by incorporating spatially more global constraints computed from lateral multigrid correlations.

LEAST-SQUARES HORIZONS WITH MULTIGRID CORRELATIONS

Because local reflection slopes, computed from structure tensors or other methods (e.g., Fomel, 2002; Marfurt, 2006; Yu et al., 2013; Arias, 2016), are often inaccurate in discontinuous areas with noise, chaotic reflections, or faults, the horizon extraction method based on only local slopes often fail to correctly follow reflections across these areas, as shown in Figure 3a and 3b. However, the reflections across these areas can be correctly followed by directly correlating the seismic traces on the opposite sides of the discontinuous areas, as shown in Figure 1d. Based on these observations, we improve the iterative horizon extraction (Figures 3c and 4d) by fitting a horizon, in the least-squares sense, with the local reflection slopes and spatially more global reflection correlations.

Multigrid correlations

As shown in Figure 3a, by starting from seed points and recursively following or accumulating local reflection slopes, we may fail to correctly track the reflections far away from the seed points. Therefore, to correlate reflections that are spatially far away from each other, we also directly correlate the seismic traces in laterally coarser grids, as shown in Figure 1d.

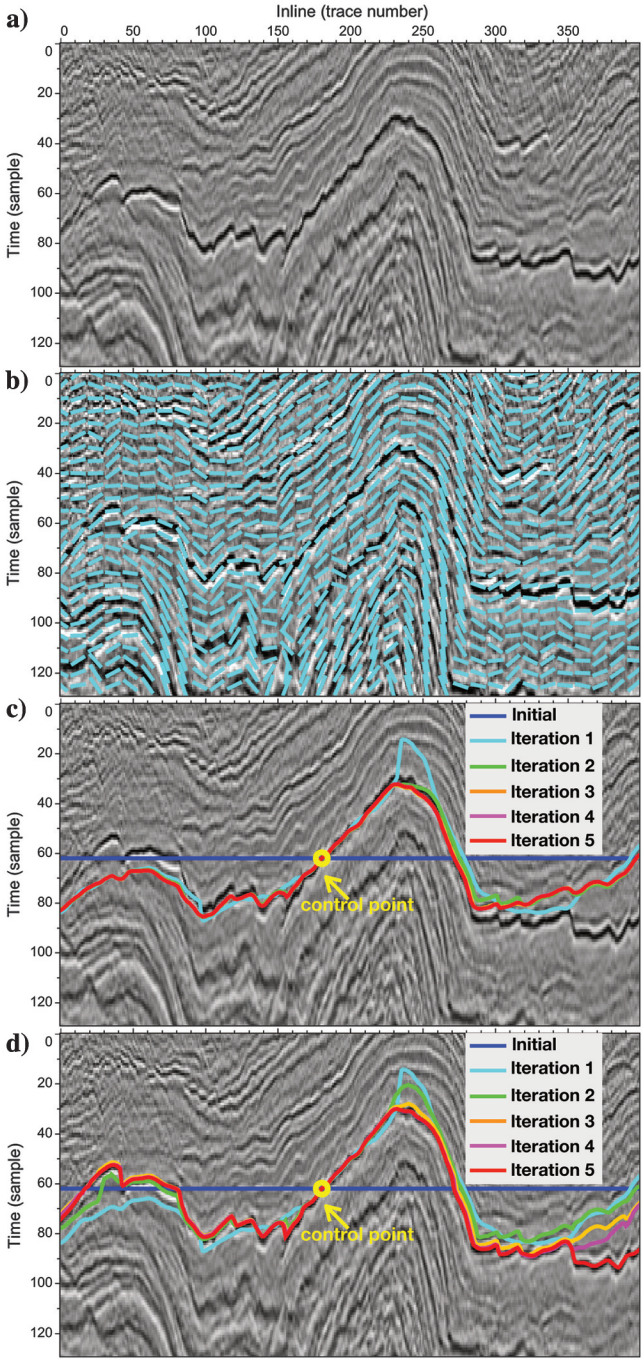

Figure 4. (a) A 2D seismic image is displayed with (b) local slope vectors, (c) five iterations of a horizon computed by least-squares fitting with only local slopes, and (d) local slopes and multigrid correlations.

Figure 5 displays pair-wise correlations of seismic traces in multiple laterally coarse grids of the example shown in Figure 4. In this example, we totally have 380 traces in the lateral inline direction. We first choose laterally sparse traces $s_j(z)$ ($j \in \mathcal{J} = \{0, 20, 40, \ldots, 380\}$), one for every 20 traces, as shown in Figure 5a. We then compute pair-wise correlations of these traces by using DTW, similar in computing pair-wise well-log correlations discussed by Wheeler and Hale (2014). To reduce computational cost, we do not compute all possible pair-wise correlations as discussed by Wheeler and Hale (2014). Instead, we only compute correlations of those pairs denoted by the black curves in Figure 5a–5c, where the lateral distance of each pair ($s_k(z)$ and $s_l(z)$, $k, l \in \mathcal{J}$) are $|l-k| = 20$ traces (Figure 5a), $|l-k| = 40$ traces (Figure 5b), and $|l-k| = 60$ traces (Figure 5c), respectively. As denoted by the blue curves in Figure 5d, we also compute pair-wise correlations of the reference trace (at the control point) with all the other traces in the coarse grid with an interval of 20 traces. We compute the correlation of each pair of traces by using DTW (Hale, 2013), as shown in Figure 2.

To improve the efficiency of the pair-wise correlations, we do not vertically correlate the traces in the entire sampling range of depth or time. Instead, we compute correlations of the traces only in a small depth window centered at the horizon. The cyan curve in Figure 6a shows the horizon updated at the first iteration. The vertical yellow or red segments represent vertical depth windows, each of which contains only 70 depth samples and is vertical centered at the horizon. Horizontally, these depth windows are evenly placed in a coarse grid of every 20 traces. We extract seismic traces within these depth windows and flatten the traces with the centered cyan horizon $z_i(x)$ to obtain the flattened traces $s_j(\tau)$ shown in Figure 6b, where τ represents the vertical axis in the flattened space.

With these flattened short traces, we compute their pair-wise correlations within horizontally multiple coarse grids, as illustrated in

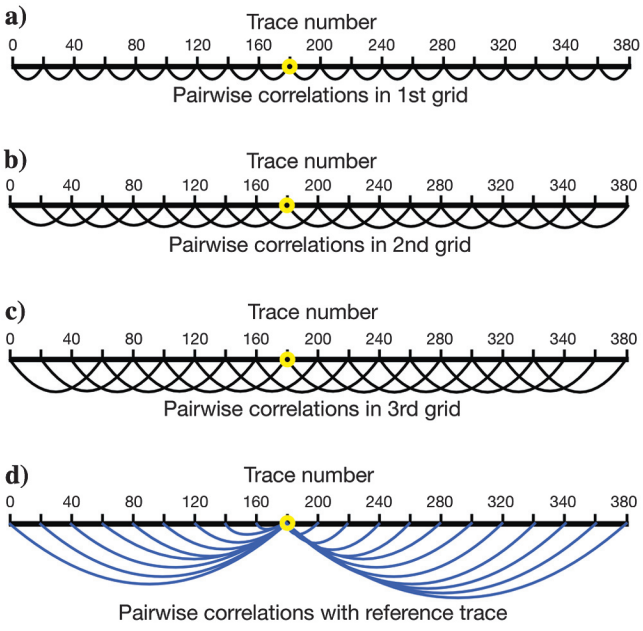

Figure 5. The black curves in (a-c) denote the pair-wise correlations of seismic traces on multiple coarse grids, where the lateral distances of each pair in (a-c) are 20, 40, and 60 traces, respectively. The blue curves in (d) denote pair-wise correlations of the reference trace (denoted by the yellow circle) with all the other traces.

Figure 5. We compute each pair-wise correlation of the traces using DTW as shown in Figure 2. From the relative correlation shifts $u_{k,l}(\tau)$ computed for each pair of traces ($s_k(\tau)$ and $s_l(\tau)$, $k, l \in \mathcal{J}$) within multiple coarse grids $|l-k| = 20$, 40, or 60, we are able to estimate the corresponding multigrid reflection slopes $p_{k,l}(z)$.

In equation 11 of updating a horizon at each $(i+1)$th iteration, we only need to compute slopes at the previous horizon $z_i(x)$ updated at the ith iteration. Therefore, with the relative shifts $u_{k,l}(\tau)$ of the multigrid pair-wise correlations, we also compute the corresponding multigrid slopes $p_{k,l}(z_i)$ only at horizon $z_i(x)$:

$$p_{k,l}(z_i) = \frac{u_{k,l}(\tau = 0)}{l-k} + \frac{z_i(x_l) - z_i(x_k)}{l-k}, \tag{17}$$

where $x_k = k$ and $x_l = l$ represent the lateral (inline or crossline) indexes of the seismic traces extracted on a laterally coarse grid $k, l \in \mathcal{J} = \{0, 20, 40, \ldots, 380\}$ as shown in Figures 5 and 6. The term $u_{k,l}(\tau = 0)$ represents the correlation shifts at the horizon z_i in the flattened space, where the horizon is flattened as a horizontal line at $\tau = 0$ (the colorful horizontal line in Figure 6b–6f). As the pair-wise correlations are computed in the flattened space, the horizon slope $([z_i(l) - z_i(k)]/(l-k))$ is added to the correlation shifts to obtain the multigrid slopes $p_{k,l}(z_i)$ in the original (unflattened) space.

As illustrated in Figure 5d, we also compute pair-wise correlations between the reference trace $s_c(\tau)$ and all the other traces $s_j(\tau), j \in \mathcal{J}$ in the flattened space τ. Reference trace $s_c(\tau)$ is the seismic trace containing the control point and colored by red in Figure 6b–6f. Similarly, by using the pair-wise correlation shifts $u_{c,j}(\tau)$ of the reference and all the other traces, we can compute the corresponding coarse-grid slopes $p_{c,j}(z_i)$ at the horizon $z_i(x)$ as

$$p_{c,j}(z_i) = \frac{u_{c,j}(\tau = 0)}{j-c} + \frac{z_i(x_j) - z_i(x_c)}{j-c}. \tag{18}$$

Least-squares horizons with multigrid slopes

By incorporating the estimated multigrid slopes $p_{k,l}(z_i)$ and $p_{c,j}(z_i)$ into equation 11 of horizon updating, we solve the least-squares solution of the following larger system at each iteration to update the horizon:

$$\begin{bmatrix} w(x, z_i)\frac{\partial z_{i+1}}{\partial x} \\ \lambda w_{k,l}\frac{z_{i+1}(l) - z_{i+1}(k)}{l-k} \\ \lambda w_{c,j}\frac{z_{i+1}(j) - z_{i+1}(c)}{j-c} \\ \mu\frac{\partial^2 z_{i+1}(x)}{\partial x^2} \end{bmatrix} \approx \begin{bmatrix} w(x, z_i)p(x, z_i) \\ \lambda w_{k,l}p_{k,l}(z_i) \\ \lambda w_{c,j}p_{c,j}(z_i) \\ 0 \end{bmatrix}, \tag{19}$$

where the first three equations indicate that we expect the horizon slopes to be approximately equal to the local reflection slopes $p(x, z_i(x))$ and multigrid slopes $p_{k,l}(z_i)$ and $p_{c,j}(z_i)$. The function λ is a small constant number used to balance the first three equations. The weights $w_{k,l}$ and $w_{c,j}$ are defined as

$$w_{k,l} = \frac{w(k, z_i(k)) + w(l, z_i(l))}{2} \tag{20}$$

and

$$w_{c,j} = \frac{w(c, z_i(c)) + w(j, z_i(j))}{2}. \tag{21}$$

In equations 19, the local reflection slopes and multigrid slopes are independently estimated using structure tensors and pair-wise

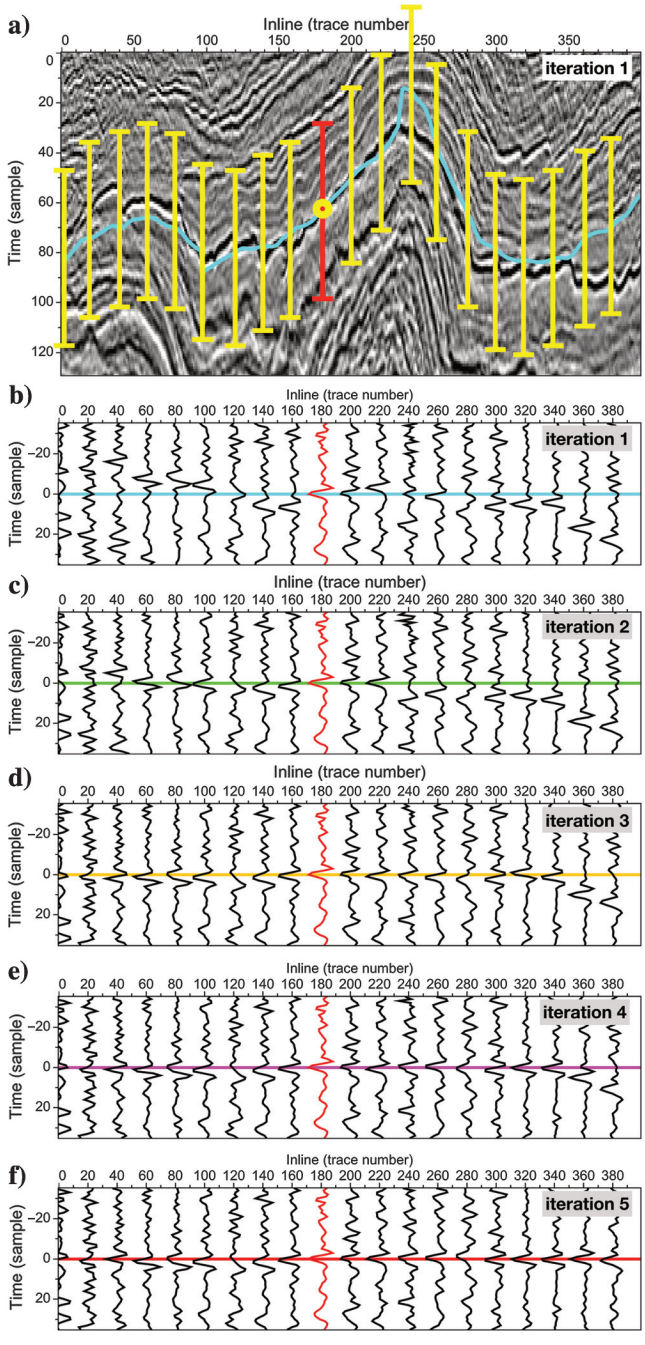

Figure 6. From the seismic image in (a), we extract horizontally sparse (one for every 20 traces) traces within vertical short windows (yellow and red segments) that are centered at the iteratively updating horizon (cyan curve in [a] denote the horizon at the first iteration). These traces are flattened by the updating horizon at the (b) first, (c) second, (d) third, (e) fourth, and (f) fifth iterations. At the final (fifth) iteration, all the traces are horizontally aligned and the flattened horizon (red line) in the middle consistently passes through all the troughs.

correlations; these slopes will provide independent and multiscale constraints in updating the horizon. In cases in which the local slopes cannot correctly follow reflections across faults, the coarse-grid slopes will be helpful to correct the errors and find the correct correlation of the reflections across faults as shown in Figure 1d.

By instituting the coarse-grid slope equations 17 and 18 into the above equation 19, we can simplify this equation 19 as

$$\begin{bmatrix} w(x,z_i)\frac{\partial z_{i+1}}{\partial x} \\ \lambda w_{k,l}[z_{i+1}(l)-z_{i+1}(k)] \\ \lambda w_{c,j}[z_{i+1}(j)-z_{i+1}(c)] \\ \mu\frac{\partial^2 z_{i+1}(x)}{\partial x^2} \end{bmatrix} \approx \begin{bmatrix} w(x,z_i)p(x,z_i) \\ \lambda w_{k,l}[u_{k,l}(z_i)+z_i(l)-z_i(k)] \\ \lambda w_{c,j}[u_{c,j}(z_i)+z_i(j)-z_i(c)] \\ 0 \end{bmatrix}. \tag{22}$$

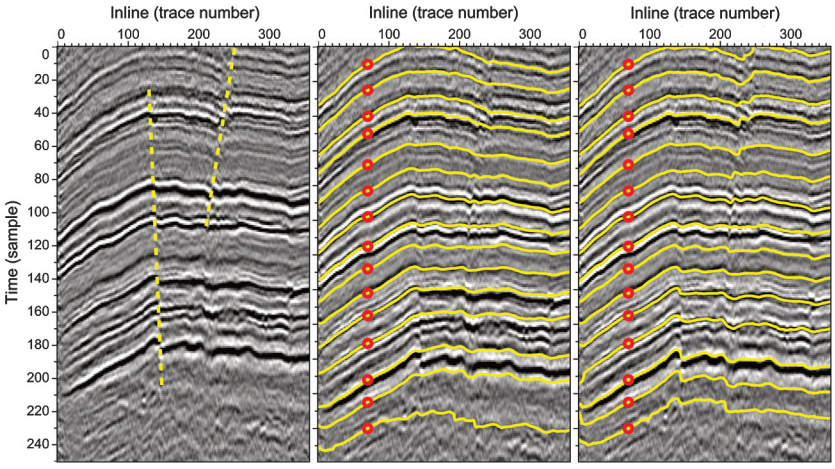

Figure 7. (a) A 2D seismic image is displayed with horizons that are extracted by computing (b) the least-squares fit of only local slopes and (c) local slopes and multigrid correlations, respectively. With multigrid correlations, we are able to correctly extract horizons across faults without the need of detecting fault positions and estimating fault slips.

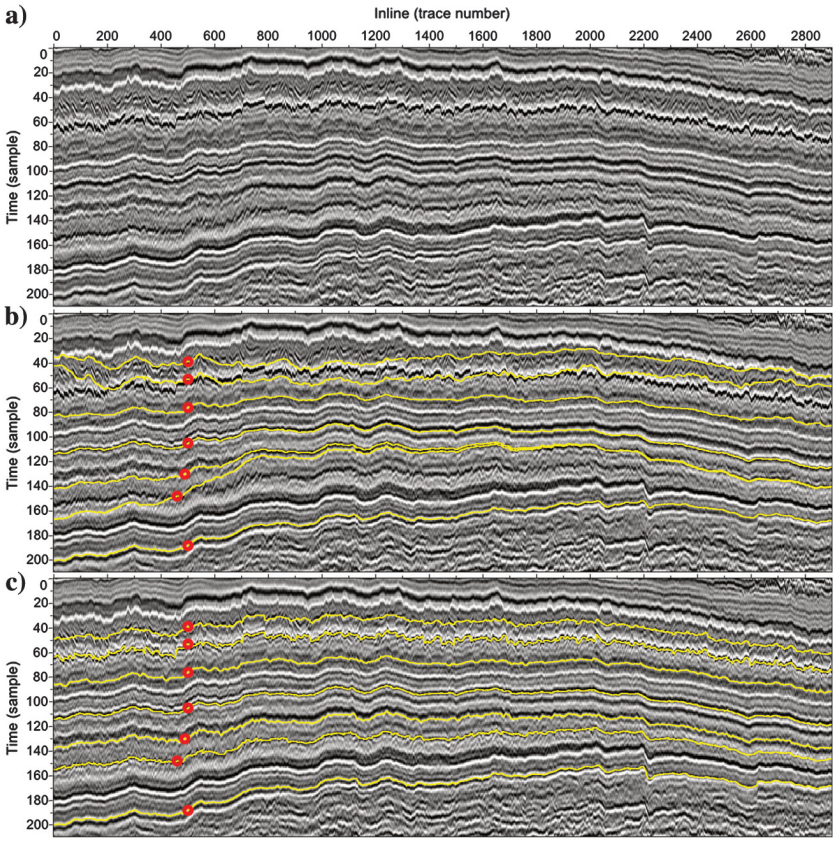

Figure 8. (a) Because of the numerous faults in the seismic image, the method with only local slopes (equation 11) fails to accurately extract horizons as shown in (b). By using the method with multigrid slopes (equation 19), the extracted horizons in (c) accurately follow consistent phase (peaks or troughs) and correctly track reflections across faults without picking the faults and estimating fault slips.

Figure 4b and 4c, respectively, shows the five iterations of horizon extraction using only local slopes (equation 11) and multigrid slopes (equation 22). With only local slopes, the horizon in Figure 4b stops updating at the third iteration but it does not converge to the correct position. This indicates that the iterative horizon updating is stuck at a local minima due to the local slope errors near faults. With multigrid slopes, the horizon in Figure 4c keeps updating until it converges to the correct position at the fifth iteration, where the coarse-grid slopes or correlations provide laterally global correlations across faults to correct local slope errors near faults. The third equation is also trying to correlate all the reflections of a horizon to the reflection at the control point, which is helpful to avoid error propagation in directions away from the control point.

Figure 6b–6f shows the five iterations of the updating horizon with multigrid slopes and the seismic traces on a laterally coarse grid with an interval of 20 traces. These traces are centered at the updating horizon at each iteration and are flattened by the horizon, which is flat in Figure 6b–6f. Within these five iterations shown in Figure 6b–6f, we can observe that the seismic traces are gradually aligned to the reference trace (the 180th trace denoted in red in Figure 6) at the control point (denoted by the yellow circle in Figures 4 and 6a). At the final iteration (Figure 6f), all the seismic traces are horizontally aligned. This means that the correlation shifts ($u_{k,l}(\tau)$ and $u_{c,j}(\tau)$ in equations 17 and 18) of these traces will be equal to zeros; then, we have $z_{i+1}(l)-z_{i+1}(k)=z_i(l)-z_i(k)$ and $z_{i+1}(c)-z_{i+1}(j)=z_i(c)-z_i(j)$ in equation 22, which indicates that the horizon is already converged because the multigrid slopes of the horizon at the $(i+1)$th and ith iterations are already identical and no more updates are required. We also observe the final horizon (the red line flattened in Figure 6f) consistently passes through all troughs of the

traces, which indicates that the multigrid slopes computed by DTW are also helpful to compute horizons following a consistent seismic phase.

Extending the horizon extraction with multigrid slopes from two dimensions to three dimensions is quite straightforward. In 3D cases, we compute the pair-wise correlation of seismic traces within multiple coarse grids in the inline and crossline directions to estimate multigrid inline and crossline slopes, with which we solve the least-squares solution of the following equations at each iteration to update the horizon $z_i(x,y)$:

$$\begin{bmatrix} w(x,y,z_i)\frac{\partial z_{i+1}}{\partial x} \\ w(x,y,z_i)\frac{\partial z_{i+1}}{\partial y} \\ \lambda w_{k,l}(y,z_i)\frac{z_{i+1}(l,y)-z_{i+1}(k,y)}{l-k} \\ \lambda w_{c,j}(y,z_i)\frac{z_{i+1}(c,y)-z_{i+1}(j,y)}{j-c} \\ \lambda w_{k,l}(x,z_i)\frac{z_{i+1}(x,l)-z_{i+1}(x,k)}{l-k} \\ \lambda w_{c,j}(x,z_i)\frac{z_{i+1}(x,c)-z_{i+1}(x,j)}{j-c} \\ \mu\left(\frac{\partial^2 z_{i+1}}{\partial x^2}+\frac{\partial^2 z_{i+1}}{\partial y^2}\right) \end{bmatrix} \approx \begin{bmatrix} w(x,y,z_i)p(x,y,z_i) \\ w(x,y,z_i)q(x,y,z_i) \\ \lambda w_{k,l}(y,z_i)p_{k,l}(y,z_i) \\ \lambda w_{c,j}(y,z_i)p_{c,j}(y,z_i) \\ \lambda w_{k,l}(x,z_i)q_{k,l}(x,z_i) \\ \lambda w_{c,j}(x,z_i)q_{c,j}(x,z_i) \\ 0 \end{bmatrix}, \tag{23}$$

where $p_{k,l}(y,z_i)$ and $q_{k,l}(x,z_i)$, respectively, represent the coarse-grid slopes computed from the pair-wise correlations of traces on lateral coarse grids (j,y) and (x,j) in the inline and crossline directions, respectively. $j \in \mathcal{J} = \{0, 20, 40, \dots\}$ and the lateral distances of the pairs $k, l \in \mathcal{J}$ are defined as $|l-k| = 20$, 40, and 60. In practice, we can choose different lateral coarse grids (j,y) and (x,j) with $j \in \mathcal{J} = \{0, 10, 20, 30, \dots\}$ and different distances of the pairs, for example $|l-k| = 10$, 30, 40, and 60. Compared with the 3D horizon surface extraction with only local slopes in equation 15, a lot more equations from multigrid slopes are incorporated to provide laterally global constraints for horizon extraction.

APPLICATIONS

The 2D examples in Figures 1 and 4 already show that the proposed method with local reflections slopes and multigrid slopes or correlations can generate much more accurate horizons across faults than the conventional method with only local slopes. To further demonstrate the superiority of the method with multigrid slopes compared with the one with only local slopes, we apply the methods to more 2D and 3D examples complicated by faults.

2D applications

Figure 7a shows a 2D seismic image extracted from the Teapot Dome survey, which was provided by the Rocky Mountain Oilfield Testing Center. The structures in this seismic image are quite simple, but the two faults (the dashed yellow lines Figure 7a) still make the method with only local slopes (equation 11) fail to correctly extract horizons (the yellow curves in Figure 7b) across these two faults. By using the method with multigrid slopes, all the extracted horizons correctly follow reflections across faults as shown in Figure 7c. In both methods, we use the same control points (denoted by the red circles), one for each horizon, and we did not try to detect faults to constrain the horizon computation.

Figure 8a shows a more complicated 2D seismic image, where numerous local faults make the reflections highly discontinuous. In this case, the local slopes estimated from structure tensors or other methods will fail to follow these laterally discontinuous reflections. Due to the errors in local slopes, the horizons (especially the first, second, and sixth horizons in Figure 8b) extracted by fitting only local slopes completely fail to track geologically consistent reflections. However, by using the method with multigrid slopes, we are able to accurately extract all the horizons in Figure 8c without the need of detecting faults and estimating fault slips. We can observe that all the extracted horizons in Figure 8c accurately follow consistent phases such as peaks or troughs.

3D applications

Figure 9 shows a 3D subset (951 [inline] × 550 [crossline] × 242 [time] samples) of the Netherlands offshore F3 block seismic data. This 3D seismic image is complicated by faults and salt bodies at the bottom of the image. The yellow and black arrows denote the two horizons that we expect to extract using the methods with only local slopes and multigrid slopes.

The first horizon (denoted by the yellow arrows in Figure 9) is complicated by a large fault (denoted by the yellow line in Figure 9) and a lot of dewatering faults, which make the horizon highly discontinuous. By using the method with the least-squares fitting of only local slopes (equation 15), we extract the horizon surface in Figure 10a (colored by amplitudes) with one control point (denoted by the small green cube in Figure 10a). This extracted horizon follows the general structure trend, but we can observe significantly amplitude variations on the surface. Because the control point is picked at an amplitude trough, we expect the horizon surface to pass through amplitude troughs and the surface should be colored red (negative values) everywhere. The blue areas on the horizon surface (Figure 10a) indicate that the extracted horizon does not correctly follow seismic amplitude troughs and jumps to peaks within these areas. By using the method with least-squares fitting of the local reflection slopes and multigrid slopes (equation 23), we compute a horizon surface shown

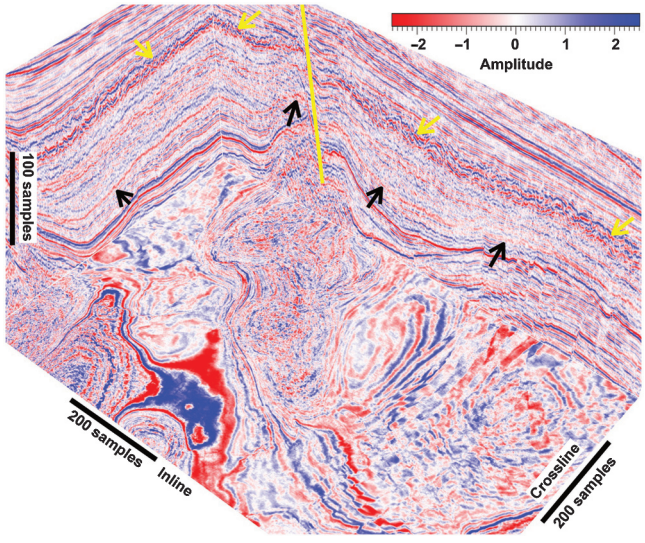

Figure 9. A 3D seismic image with faults (yellow line) and salt bodies (at the bottom of the image). The yellow and black arrows denote the two horizons that we want to extract.

in Figure 10b. This extracted horizon is colored red almost everywhere, which indicates that this horizon follows consistent troughs and is much more accurate than the one shown in Figure 10a. On the extracted horizon shown in Figure 10b, we can clearly observe a lot of discontinuous dewatering structures, but the horizon still reasonably follows the seismic amplitude troughs as expected.

The second horizon (denoted by the black arrows in Figure 9) is complicated by the large fault (denoted by the yellow line in Figure 9) and a large salt body at the bottom of the image. To extract this horizon surface, we use two control points (denoted by the small green cubes in Figure 11) on two sides of the salt body. Figure 11a shows the horizon surface computed by using the method with only local slopes (equation 15). This extracted horizon, again, is not accurate enough because we can observe blue and red areas on the surface, which indicates that the horizon jumps from troughs to peaks. The two control points are, again, picked at amplitude troughs, an ideal horizon should constantly follow amplitude troughs and therefore should be colored red almost everywhere.

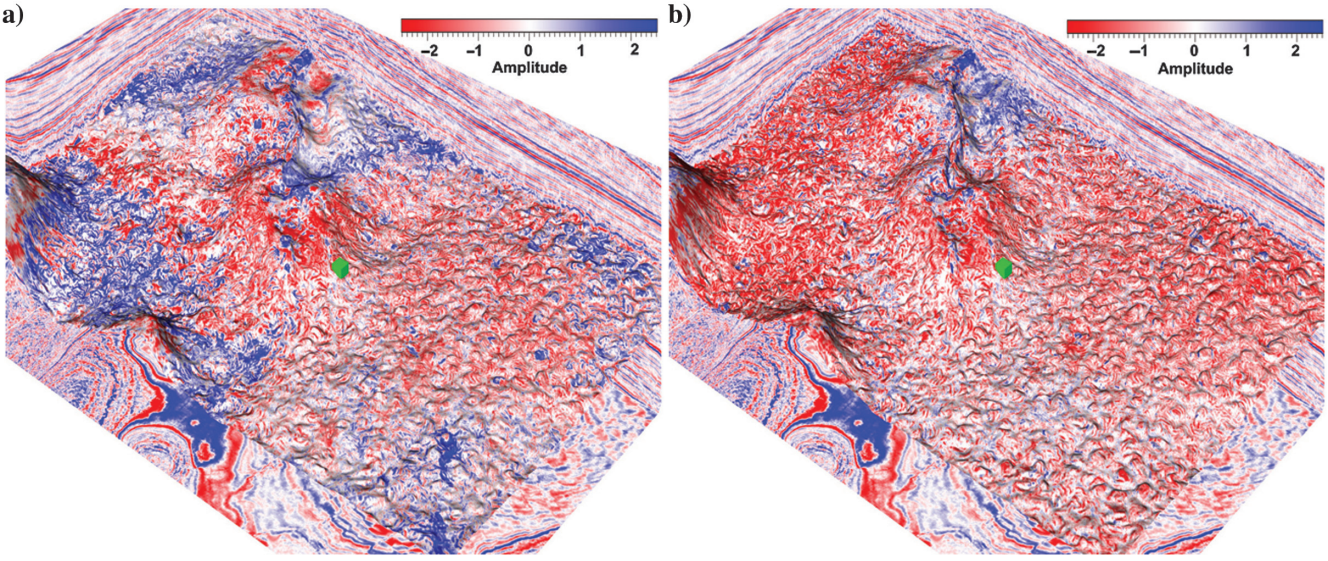

Figure 10. From the 3D seismic image (Figure 9), the two horizon surfaces in (a and b) are computed by using the methods with only local slopes and local slopes and multigrid correlations, respectively. Both of the surfaces are computed by using one control point denoted by the green point. Both of the surfaces are colored by amplitude, and the amplitude values on the surface in (b) are more consistent than those on the surface in (a).

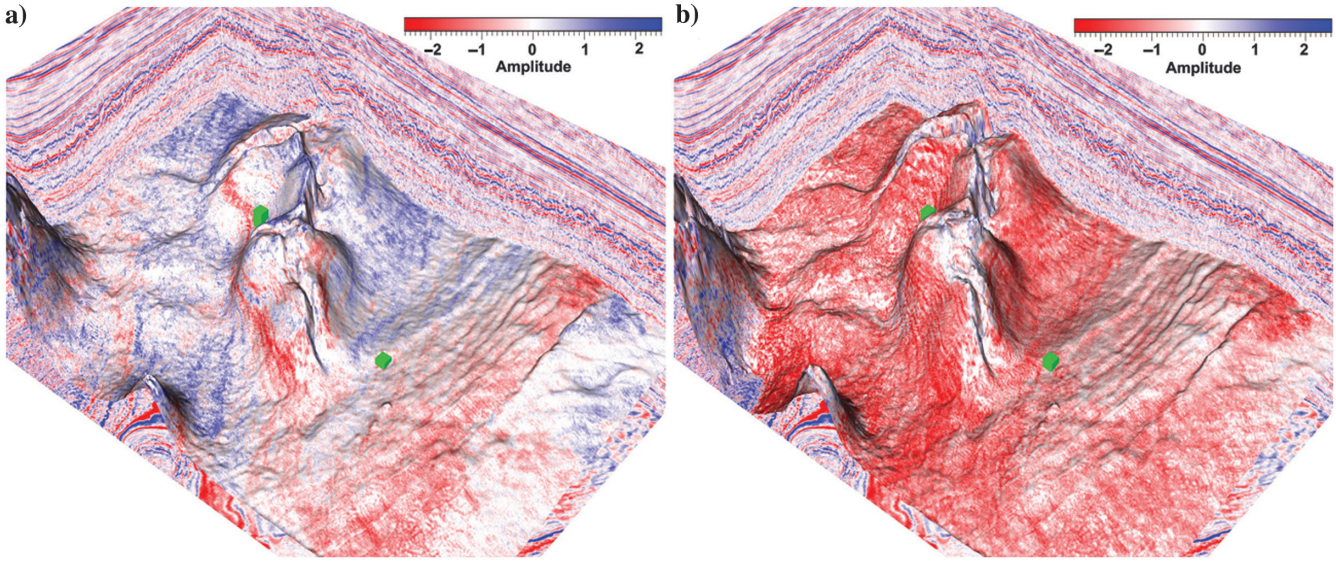

Figure 11. From the 3D seismic image (Figure 9), the two horizon surfaces in (a and b) are computed by using the methods with only local slopes and local slopes and multigrid correlations, respectively. Both of the surfaces are computed by using two control points denoted by the green points on the two sides of a salt body. Both of the surfaces are colored by amplitude, and the amplitude values on the surface in (b) are more consistent than those on the surface in (a).

In Figure 11b, the method with local reflection slopes and multigrid slopes yields such an ideal horizon that we expect. We can observe that this horizon is complicatedly folded by the salt body and the large faults related to the salt body, but the computed horizon Figure 11b still reasonably follows seismic amplitude troughs and is colored red almost everywhere.

The method with local slopes and multigrid slopes is computationally more expensive than the one with only local slopes because the former requires computing multigrid slopes at each iteration and solving a larger least-squares system. In this example, the method with only local slopes took approximately 1 min to compute each of the horizons shown in Figures 10a and 11a by using an eight-core computer. By using the same computer, the method with local slopes and multigrid slopes took approximately 3 min to compute each of the horizons shown in Figures 10b and 11b.

Figure 12a shows another large 3D seismic volume (880 (inline) × 1325 (crossline) × 500 (time) samples) provided by the Reservoir Characterization Research Laboratory (RCRL consortium at the Bureau of Economic Geology), who purchased the data from Australian Government-Geoscience Australia. This seismic volume is complicated by dramatically varying foldings caused by channel valleys as shown in the vertical sections. Figure 12b shows a horizon surface that is extracted by using the method with multigrid slopes and using only one control point (denoted by the small green cube) picked at an amplitude peak. This extracted horizon surface is colored by white almost everywhere, which indicates that the horizon reasonably follows amplitude peaks. From this horizon surface, we can clearly observe a lot of interesting geologic features including large canyons, relatively smaller channels, and alluvial fans.

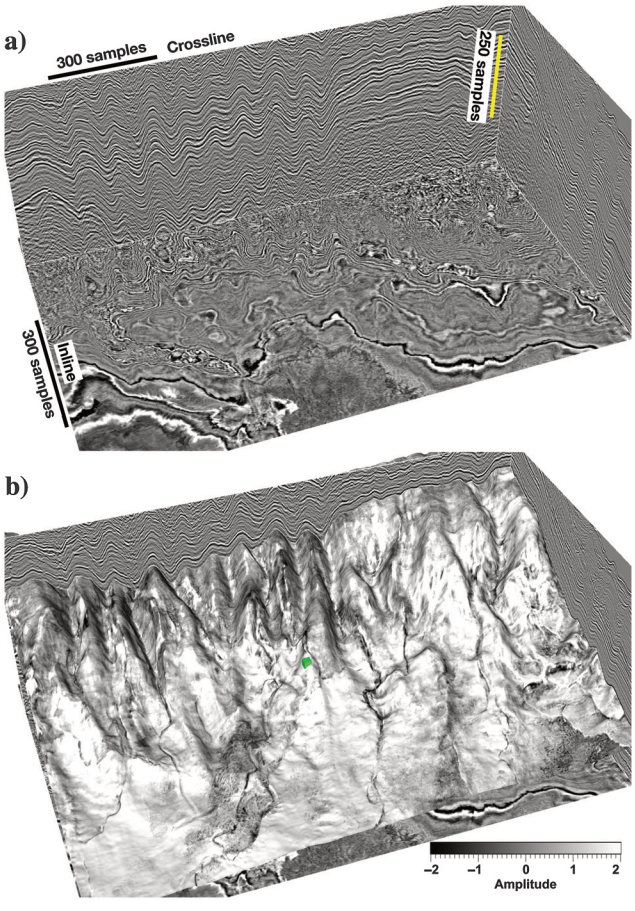

Figure 12. (a) From the 3D seismic image, (b) a horizon surface is computed by using only one control point (green point in [b]) in the method with local slopes and multigrid correlations. This surface is colored by seismic amplitude.

CONCLUSION

We have discussed iterative horizon extraction methods based on local reflection slopes and multigrid slopes or correlations. At each iteration of the methods, we fit, in the least-squares sense, the slopes of a horizon with local reflection slopes and multigrid slopes.

We estimate the local reflection slopes on a fine grid by using the structure-tensor method. The local slopes can correctly follow laterally continuous reflections but fail to correlate reflections across faults. In addition, these local reflection slopes do not necessarily follow consistent phases and may jump from peaks to troughs (or troughs to peaks). We estimate multigrid slopes by directly correlating seismic traces on multiple laterally coarse grids using DTW. When the traces on the coarse grids are located on the opposite sides of a fault, the correlations of these traces can be helpful to correctly track corresponding reflections on the opposite sides of a fault. In addition, by using the amplitude-based DTW, the computed multigrid slopes or correlations can provide more accurate phase correlations than the local reflection slopes to compute a horizon following consistent phase. To increase the efficiency of estimating the multigrid slopes, we do not correlate seismic traces within the whole time or depth window; instead, we only correlate the traces in a small time or depth window centered at the iteratively updating horizon.

By least-squares fitting, the horizon slopes with only local reflection slopes, the horizon extraction method fails to track horizons across faults because the local slopes cannot correctly correlate reflections across faults. Therefore, we suggest to fit the horizon slopes with the local reflection slopes and multiple coarse-grid slopes. Near the faults where local slopes fail to follow reflections, we weight the slopes with low-reflection linearity or planarity that is computed at the same time as estimating the reflection slopes by using structure tensors. The coarse-grid slopes that correctly correlate reflections on the opposite sides of the faults will contribute the most in the least-squares fitting to yield an accurate horizon that correctly tracks reflections across faults and follows consistent phase. This horizon extraction method with local slopes and multigrid slopes can be further extended to flatten a seismic volume to simultaneously obtain all seismic horizons within the volume.

ACKNOWLEDGMENTS

This research is financially supported by the sponsors of the Texas Consortium for Computation Seismology.

REFERENCES

Arias, E., 2016, Estimating seismic reflection slopes: Master's thesis, Colorado School of Mines.

Bakker, P., 2002, Image structure analysis for seismic interpretation: Ph.D. thesis, Delft University of Technology.

Bakker, P., L. J. van Vliet, and P. W. Verbeek, 1999, Edge preserving orientation adaptive filtering: Proceedings of the IEEE Computer Society Conference on Computer Vision and Pattern Recognition.

Fehmers, G. C., and C. F. Höcker, 2003, Fast structural interpretation with structure-oriented filtering: Geophysics, **68**, 1286–1293, doi: 10.1190/1.1598121.

Figueiredo, A. M., M. Gattass, and F. Szenberg, 2007, Seismic horizon mapping across faults with growing neural gas: 10th International Congress of the Brazilian Geophysical Society & EXPOGEF 2007, 1476–1481.

Figueiredo, A. M., P. M. Silva, M. Gattass, F. B. Silva, and R. L. Milidiú, 2014, A seismic faces analysis approach to map 3D seismic horizons: 84th Annual International Meeting, SEG, Expanded Abstracts, 1501–1505.

Figueiredo, A. M., F. B. Silva, P. Silva, L. de O. Martins, R. L. Milidiú, and M. Gattass, 2015, A clustering-based approach to map 3D seismic horizons: 14th International Congress of the Brazilian Geophysical Society & EXPOGEF, 1166–1170.

Fomel, S., 2002, Applications of plane-wave destruction filters: Geophysics, **67**, 1946–1960, doi: 10.1190/1.1527095.

Fomel, S., 2010, Predictive painting of 3D seismic volumes: Geophysics, **75**, no. 4, A25–A30, doi: 10.1190/1.3453847.

Fomel, S., and L. Jin, 2009, Time-lapse image registration using the local similarity attribute: Geophysics, **74**, no. 2, A7–A11, doi: 10.1190/1.3054136.

Hale, D., 2006, Recursive Gaussian filters: CWP-546, Colorado School of Mines.

Hale, D., 2009a, A method for estimating apparent displacement vectors from time-lapse seismic images: Geophysics, **74**, no. 5, V99–V107, doi: 10.1190/1.3184015.

Hale, D., 2009b, Structure-oriented smoothing and semblance: CWP Report 635, Colorado School of Mines.

Hale, D., 2013, Dynamic warping of seismic images: Geophysics, **78**, no. 2, S105–S115, doi: 10.1190/geo2012-0327.1.

Herrera, R. H., and M. van der Baan, 2014, A semiautomatic method to tie well logs to seismic data: Geophysics, **79**, no. 3, V47–V54, doi: 10.1190/geo2013-0248.1.

Julio, C., F. Lallier, and G. Caumon, 2012, Accounting for seismic trends in stochastic well correlation, *in* P. Abrahamsen, R. Hauge, and O. Kolbjørnsen, eds., Geostatistics, Oslo 2012: Springer, Quantitative Geology and Geostatistics, 251–262.

Lomask, J., A. Guitton, S. Fomel, J. Claerbout, and A. A. Valenciano, 2006, Flattening without picking: Geophysics, **71**, no. 4, P13–P20, doi: 10.1190/1.2210848.

Luo, S., and D. Hale, 2013, Unfaulting and unfolding 3D seismic images: Geophysics, **78**, no. 4, O45–O56, doi: 10.1190/geo2012-0350.1.

Marfurt, K. J., 2006, Robust estimates of 3D reflector dip and azimuth: Geophysics, **71**, no. 4, P29–P40, doi: 10.1190/1.2213049.

Monniron, M., S. Frambati, S. Quillón, Y. Berthoumieu, and M. Donias, 2016, Seismic horizon and pseudo-geological time cube extraction based on a Riemmanian geodesic search: Presented at the IEEE 12th Image, Video, and Multidimensional Signal Processing Workshop (IVMSP).

Parks, D., 2010, Seismic image flattening as a linear inverse problem: Master's thesis, Colorado School of Mines.

Posamentier, H., R. Davies, J. Cartwright, and L. Wood, 2007, Seismic geomorphology: An overview, *in* R. J. Davies, H. W. Posamentier, L. J. Wood, and J. A. Cartwright, eds., Seismic geomorphology: Geological Society of London, Special Publications, 1–14.

Sakoe, H., and S. Chiba, 1978, Dynamic programming algorithm optimization for spoken word recognition: IEEE Transactions on Acoustics, Speech, and Signal Processing, **26**, 43–49, doi: 10.1109/TASSP.1978.1163055.

Smith, T., and M. Waterman, 1980, New stratigraphic correlation techniques: The Journal of Geology, **88**, 451–457, doi: 10.1086/628528.

Stark, T. J., 2003, Unwrapping instantaneous phase to generate a relative geologic time volume: 73rd Annual International Meeting, SEG, Expanded Abstracts, 1707–1710.

Stark, T. J., 2004, Relative geologic time (age) volumes — Relating every seismic sample to a geologically reasonable horizon: The Leading Edge, **23**, 928–932, doi: 10.1190/1.1803505.

Stark, T. J., 2005, Generating a seismic Wheeler volume: 75th Annual International Meeting, SEG, Expanded Abstracts, 782–785.

Vail, P. R., R. G. Todd, and J. B. Sangree, 1977, Seismic stratigraphy and global changes of sea level. Part 5: Chronostratigraphic significance of seismic reflections: Section 2. Application of seismic reflection configuration to stratigraphic interpretation: M 26, *in* C. E. Payton, ed., Seismic stratigraphy — Applications to hydrocarbon exploration: AAPG Memoirs, 99–116.

Van Vliet, L. J., and P. W. Verbeek, 1995, Estimators for orientation and anisotropy in digitized images: Proceedings of the First Annual Conference of the Advanced School for Computing and Imaging ASCI'95, 442–450.

Weickert, J., 1997, A review of nonlinear diffusion filtering, *in* B. ter Haar Romeny, L. Florack, J. Koenderink, and M. Viergever, eds., Scale-space theory in computer vision: Springer, Lecture Notes in Computer Science, doi: 10.1007/3-540-63167-4_37.

Wheeler, L., and D. Hale, 2014, Simultaneous correlation of multiple well logs: 84th Annual International Meeting, SEG, Expanded Abstracts, 618–622.

Wu, X., 2017, Directional structure-tensor based coherence to detect seismic faults and channels: Geophysics, **82**, no. 2, A13–A17, doi: 10.1190/geo2016-0473.1.

Wu, X., and G. Caumon, 2017, Simultaneous multiple well-seismic ties using flattened synthetic and real seismograms: Geophysics, **82**, no. 1, IM13–IM20, doi: 10.1190/geo2016-0295.1.

Wu, X., and D. Hale, 2013, Extracting horizons and sequence boundaries from 3D seismic images: 83rd Annual International Meeting, SEG, Expanded Abstracts, 1440–1445.

Wu, X., and D. Hale, 2015, Horizon volumes with interpreted constraints: Geophysics, **80**, no. 2, IM21–IM33, doi: 10.1190/geo2014-0212.1.

Wu, X., and D. Hale, 2016, Automatically interpreting all faults, unconformities, and horizons from 3D seismic images: Interpretation, **4**, no. 2, T227–T237, doi: 10.1190/INT-2015-0160.1.

Wu, X., and X. Janson, 2017, Directional structure tensors in estimating seismic structural and stratigraphic orientations: Geophysical Journal International, **210**, 534–548, doi: 10.1093/gji/ggx194.

Wu, X., S. Luo, and D. Hale, 2016, Moving faults while unfaulting 3D seismic images: Geophysics, **81**, no. 2, IM25–IM33, doi: 10.1190/geo2015-0381.1.

Wu, X., and E. Nyland, 1987, Automated stratigraphic interpretation of well-log data: Geophysics, **52**, 1665–1676, doi: 10.1190/1.1442283.

Wu, X., Y. Shi, S. Fomel, and F. Li, 2017, Incremental correlation of multiple well logs following geologically optimal neighbors: 87th Annual International Meeting, SEG, Expanded Abstracts, 1945–1949.

Wu, X., and G. Zhong, 2012, Generating a relative geologic time volume by 3D graph-cut phase unwrapping method with horizon and unconformity constraints: Geophysics, **77**, no. 4, O21–O34, doi: 10.1190/geo2011-0351.1.

Yu, Y., C. Kelley, and I. Mardanova, 2013, Volumetric seismic dip and azimuth estimation with 2D log-Gabor filter array: 83rd Annual International Meeting, SEG, Expanded Abstracts, 1357–1362.

Zinck, G., M. Donias, J. Daniel, S. Guillon, and O. Lavialle, 2013, Fast seismic horizon reconstruction based on local dip transformation: Journal of Applied Geophysics, **96**, 11–18, doi: 10.1016/j.jappgeo.2013.06.010.